Energy
Advances

ROYAL SOCIETY
OF CHEMISTRY

COMMUNICATION

View Article Online
View Journal | View Issue

Cite this: *Energy Adv.*, 2023, 2, 98

Received 23rd August 2022,
Accepted 27th November 2022

DOI: 10.1039/d2ya00223j

rsc.li/energy-advances

P3-type layered $K_{0.6}Cr_{0.6}Ti_{0.4}O_2$ for potassium storage applications†

Alok K. Pandey,[a] Benoît D.L. Campéon,[b] Itsuki Konuma[b] and Naoaki Yabuuchi *[ab]

P3-type $K_{0.6}Cr_{0.6}Ti_{0.4}O_2$ is synthesized *via* a solid-state method and is tested as a positive electrode for potassium-ion batteries. It operates at a higher potential of $E_{ave.}$ = 3.14 V *vs.* K/K$^+$, while delivering a reversible capacity superior to 40 mA h g^{-1} in a K cell. Excellent reversibility as an electrode material is achieved with a 3.9 V cutoff based on solid-state redox reaction of Cr ions. An *in situ* X-ray diffraction study reveals a reversible phase transition during K$^+$ ion extraction/insertion. Furthermore, the excellent cyclability for 500 cycles at a rate of 40 mA g^{-1} coupled with good rate capability demonstrates its advantage as the host structure for potassium ion storage applications.

Introduction

Increasing renewable energy demand has put a lot of pressure on the Li-ion battery (LIB) industry due to the limited abundance and uneven presence of lithium resources around the world.[1,2] An alternative to LIBs is deemed necessary for the future of sustainable energy storage systems. With similar intercalation chemistry, K-ion batteries (KIBs) have gained renewed attention in this regard, due to the high abundance of potassium (K^+) ions in the Earth's crust and to its relatively low cost.[3] Furthermore, the lower redox potential for potassium, E° (K/K$^+$) = −2.93 V *vs.* standard hydrogen redox potential, compared to other metallic elements such as magnesium, makes it a potential battery system for high voltage operations. The lower solvation ability of K^+ ions in organic electrolytes as compared with that of Li^+ ions also results in the development of battery applications with high-power density.[3] Recently, several materials have been reported as potential negative and positive electrodes for KIBs.[4]

Graphite can (de)intercalate K^+ ions, which satisfies the requirements for negative electrode materials.[5–7] Good electrode reversibility has also been reported for the metallic potassium electrode.[8] However, to realize the commercial application of KIBs, the development of positive electrodes with higher energy density is essential.[9,10] Layered transition metal oxides have been extensively studied as positive electrode materials for alkali metal-ion batteries because such materials offer well-defined paths in the structure, which leads to fast ion migration. In this respect, several layered oxides with K^+ ions, K_xTMO_2 (TM = 3d transition metal ions), have been reported in the past several years, including K_xMnO_2 (x = 0.3 and 0.5), K_xCoO_2 (x = 0.44 and 0.6), K_xCrO_2 (x = 0.69, 0.8, and 1), $K_{0.48}Mn_{0.4}Co_{0.6}O_2$, $K_{0.7}Fe_{0.5}Mn_{0.5}O_2$, $K_{0.45}Mn_{0.5}Co_{0.5}O_2$, $K_{0.5}Mn_{0.8}Co_{0.1}Ni_{0.1}O_2$ *etc.*[11–21] Indeed, except for $KCrO_2$, other stochiometric compounds of $KTMO_2$ form non-layered structures. This phenomenon originates from the non-compatibility between large K^+ ions and small TM ions. Large K^+ ions induce strong in-plane K^+–K^+ repulsive electrostatic interactions, which necessitates large *a* lattice parameters, while relatively small TM ions tend to favor smaller *a* lattice parameters, leading to energetic destabilization of the O3-type layered structure. Herein, "O" denotes that Li ions are accommodated at octahedral sites, and "3" denotes the number of TMO_2 layers in a unit cell.[22] In contrast, $LiCoO_2$ and $LiNiO_2$ with small Li^+ ions, which are also used for practical battery applications, crystallize into the O3-type layered structure, in which Li and TM ions sit in the two distinct octahedral sites alternately along the *c*-axis direction.[23]

In stoichiometric $KCrO_2$, however, the compound surprisingly crystallizes in the O3-type structure. The stability of O3 $KCrO_2$ is found to originate from Cr^{3+} ions having an unusual ligand field preference for the octahedral environment, which compensates for the energy penalty emerging from the short K^+–K^+ distance.[19] However, O3 $KCrO_2$ undergoes complex phase transitions during charge, and at the end of the first discharge, full reinsertion of K^+ ions is not achieved. Furthermore, inferior cycling stability and rate capability is noted as electrode materials. Instead, other

---

[a] *Department of Chemistry and Life Science, Yokohama National University, 79-5 Tokiwadai, Hodogaya-ku, Yokohama, Kanagawa 240-8501, Japan. E-mail: yabuuchi-naoaki-pw@ynu.ac.jp*

[b] *Advanced Chemical Energy Research Center, Institute of Advanced Sciences, Yokohama National University, 79-5 Tokiwadai, Hodogaya-ku, Yokohama, Kanagawa 240-8501, Japan*

† Electronic supplementary information (ESI) available. See DOI: **https://doi.org/10.1039/d2ya00223j**

K-deficient Cr-based layered metal oxides with satisfactory electrochemical performance have been reported such as P3 $K_{0.69}CrO_2$ and P′3 $K_{0.8}CrO_2$.[15,16] Unlike stochiometric O3 $KCrO_2$, in these materials, the crystallographic site of K^+ ions is prismatic ("P" denotes that K^+ ions occupy prismatic sites), which provides larger free volume compared with octahedral sites, leading to easier migration for larger K^+ ions. Nonetheless, all these Cr-based electrode materials operate at an average potential of <3.0 V. A high potential positive electrode *vs.* E° (K/K^+) is required to develop KIBs with high voltage operation. In this article, we report a Ti-substituted Cr-based layered oxide, P3 $K_{0.6}Cr_{0.6}Ti_{0.4}O_2$, as a potential positive electrode material for KIBs. Excellent reversibility for K^+ ion insertion/extraction coupled with good rate capability is achieved for P3 $K_{0.6}Cr_{0.6}Ti_{0.4}O_2$ and a higher operating voltage, superior to 3.0 V, is also demonstrated.

Results and discussion

For the synthesis of $K_xCr_xTi_{1-x}O_2$ materials, mixtures of K_2CO_3, TiO_2, and Cr_2O_3 were ball milled with ethanol and pelletized followed by calcination at 1000 °C for 5 hours in an argon atmosphere. An excess of 5% K_2CO_3 was used to compensate for potassium loss at high temperatures. After the heat treatment and cooling, the samples were immediately transferred to an argon-filled glove box. The crystal structures of the as-prepared samples were analyzed using an X-ray diffractometer (a D2 PHASER instrument, Bruker) with an airtight sample holder to prevent air/moisture exposure. Fig. 1a shows the X-ray diffraction (XRD) patterns of $K_xCr_xTi_{1-x}O_2$ materials with different chemical compositions (x = 0.4, 0.5, 0.6, and 0.65). At x = 0.4 in $K_xCr_xTi_{1-x}O_2$, an impurity phase appears along with the major P3 phase. This impurity phase can be assigned to a tunnel-type structure and is expected to be a hollandite phase. In the $0.5 \leq x \leq 0.6$ composition range, nearly single phase $K_xCr_xTi_{1-x}O_2$ compounds are successfully synthesized. Nevertheless, further increase in K^+ ion content results in segregation of the starting material, Cr_2O_3, as evidenced by the XRD pattern of $x = 0.65$. The diffraction pattern with composition x = 0.6 was analyzed by Rietveld analysis (Fig. 1b and Fig. S1, ESI†) with the RIETAN-FP program.[24] The lattice parameters were calculated to be $a_{\text{hex.}}$ = 2.968 and $c_{\text{hex.}}$ = 19.06 Å for $K_{0.6}Cr_{0.6}Ti_{0.4}O_2$ in a hexagonal setting with rhombohedral symmetry (s.g. $R\bar{3}m$) in accordance with P3 $K_{0.69}CrO_2$. However, the presence of minor impurity phases, which cannot be assigned as P3 phases, is also noted. The corresponding crystal structure schematic, which was drawn using the VESTA program,[25] is also shown as an inset in Fig. 1b. K^+ ions are accommodated in prismatic sites between (Cr, Ti)O_2 layers with the "ABBCCA" oxygen sequence. The morphological observation of the as-prepared $K_{0.6}Cr_{0.6}Ti_{0.4}O_2$ *via* field emission scanning electron microscopy (FE-SEM) (SU8010, Hitachi High-Tech) reveals that $K_{0.6}Cr_{0.6}Ti_{0.4}O_2$ consists of plate-shaped particles with a 0.5–1 μm size range exhibiting a layered structure (Fig. 1c). The energy-dispersive X-ray spectroscopy (EDX) mapping further confirms the presence and homogeneous distribution of all constituent elements. Furthermore, the layered structure of P3 $K_{0.5}Cr_{0.5}Ti_{0.5}O_2$ was directly observed at the atomic scale by high-angle annular dark-field scanning transmission electron microscopy (HAADF-STEM) as shown in Fig. 1d. The HAADF-STEM images were obtained using a JEOL JEM-ARM200F instrument with a CEOS CESCOR STEM Cs corrector (spherical aberration corrector) operated at an acceleration voltage of 200 kV. Details of the experimental setup, including specimen preparation, can be found in the literature.[26] The HAADF-STEM images show significant contrast attributed to $Cr_{0.5}Ti_{0.5}$ and K layers. In particular, the presence of Cr and Ti ions is clearly visualized and the arrangement of both ions along the *c*-axis direction is consistent with the P3-type sequence. in the in-plane and through-plane interatomic distances are also in good agreement with the lattice parameters of P3 $K_{0.5}Cr_{0.5}Ti_{0.5}O_2$ (Fig. S1, ESI†). The interlayer distances of 255 and 630 pm in Fig. 1d correspond to those of the (100) and (003) planes, respectively.

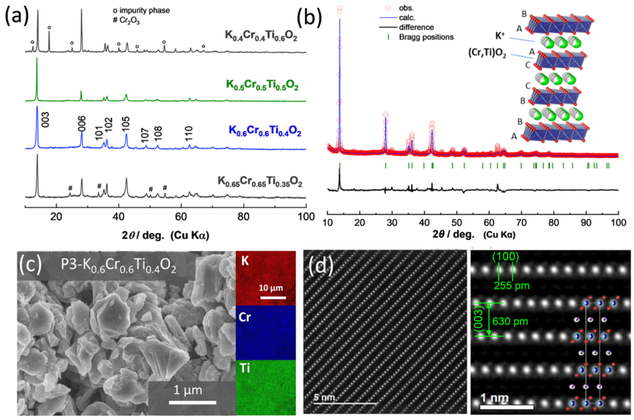

Fig. 1 Structural characterization of $K_xCr_xTi_{1-x}O_2$; (a) the XRD patterns of $K_xCr_xTi_{1-x}O_2$ with different chemical compositions, (b) the Rietveld refined XRD pattern of $K_{0.6}Cr_{0.6}Ti_{0.4}O_2$ and a schematic illustration of the P3-type layered structure is also shown in the inset, (c) the FE-SEM image and EDX maps of $K_{0.6}Cr_{0.6}Ti_{0.4}O_2$, and (d) the HAADF-STEM images of $K_{0.5}Cr_{0.5}Ti_{0.5}O_2$.

The electrochemical behavior of P3 $K_{0.6}Cr_{0.6}Ti_{0.4}O_2$ was further examined in the K cells. The composite electrode consisted of 80 wt% $K_{0.6}Cr_{0.6}Ti_{0.4}O_2$, 10 wt% acetylene black, and 10 wt% of poly(vinylidene fluoride) cast on an aluminum foil current collector. Metallic potassium was used as a counter electrode. The electrolyte solution used was 1.0 mol dm^{-3} KPF_6 in ethylene carbonate and propylene carbonate (1 : 1 in volume ratio, battery grade, Kishida Chemical). Electrochemical extraction of K^+ ions from $K_{0.6}Cr_{0.6}Ti_{0.4}O_2$ was first studied in two ranges with different higher voltage cutoffs, 3.9 and 4.3 V, with a fixed lower voltage cutoff, 2.0 V, at a rate of 5 mA g^{-1}. The galvanostatic charge/discharge at 2.0–3.9 V shows a sloping voltage profile from 2.7–3.9 V with a short voltage plateau at 2.9 V and delivers capacities of 45 and 41 mA h g^{-1} in the first charge and discharge, respectively (Fig. 2a). When the voltage cutoff was set to 3.9 V, reversible K^+ ion intercalation is achieved for subsequent cycles with a higher operating voltage of $E_{\text{ave.}}$ = 3.14 V *vs.* K/K^+. When the voltage cutoff is increased

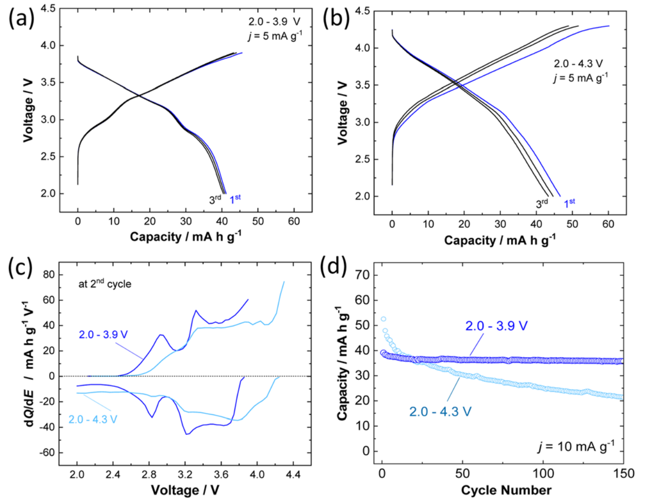

Fig. 2 Electrochemical properties of $K_{0.6}Cr_{0.6}Ti_{0.4}O_2$; (a) the charge/discharge curves of the sample in the potential window range of 2.0–3.9 V at a current rate of 5 mA g^{-1}, (b) charge/discharge profiles in the potential window range of 2.0–4.3 V, (c) dQ/dE plots at the 2nd cycle in the voltage range of 2.0–3.9 V and 2.0–4.3 V, and (d) capacity retention for 150 cycles with two distinct voltage cutoffs at a current rate of 10 mA g^{-1}.

to 4.3 V, a lowered reversibility is observed (Fig. 2b). Indeed, the first charge capacity is increased to 60 mA h g^{-1}, but the corresponding discharge capacity is limited to 46 mA h g^{-1}, resulting in a low Coulombic efficiency of 77%. When charged to 3.9 V, distinguished voltage plateaus are observed in the dQ/dE curves as shown in Fig. 2c. However, the phase transitions are clearly less pronounced when compared with O3 $K_{1-y}CrO_2$.[19] An identical trend was also reported in $Na_xCr_{1-x}Ti_xO_2$, and the presence of Ti ions, which are randomly substituted for Cr ions, effectively suppresses in-plane Na^+ ion ordering coupled with charge ordering of Cr^{3+}/Cr^{4+} ions.[27,28] Similar phenomena in the electrochemical cycles are expected for P3 $K_{0.6-y}Cr_{0.6}Ti_{0.4}O_2$. In contrast, after charging to 4.3 V, the voltage plateaus are less pronounced, resulting in a monotonous voltage profile. This observation implies that irreversible structural changes happen in the high-voltage region. Moreover, the effect of voltage cutoffs on the long-term cyclability of $K_{0.6}Cr_{0.6}Ti_{0.4}O_2$ has been evaluated at an elevated rate of 10 mA g^{-1}. The results reported in Fig. 2d show that the voltage cutoff has a tremendous effect on the capacity retention of $K_{0.6-y}Cr_{0.6}Ti_{0.4}O_2$. In the voltage range of 2.0–4.3 V, although a high discharge capacity of 53 mA h g^{-1} is obtained in the first cycle, the capacity rapidly fades to 20 mA h g^{-1} at the 150th cycle. This behavior indicates destabilization of the charged phase, including the electrolyte, during high voltage cycling. In contrast, highly reversible behavior is observed in the voltage range of 2.0–3.9 V. P3 $K_{0.6}Cr_{0.6}Ti_{0.4}O_2$ shows 94% retention even after 150 cycles. The electrochemical properties of P3 $K_{0.5}Cr_{0.5}Ti_{0.5}O_2$ are shown in Fig. S2 (ESI†). Although the reversible capacity is slightly reduced compared with $K_{0.6}Cr_{0.6}Ti_{0.4}O_2$, better capacity retention is evidenced with a 4.3 V cutoff with higher operating voltage.

To understand the K^+ ion storage mechanisms of $K_{0.6-y}Cr_{0.6}Ti_{0.4}O_2$, an *in situ* XRD study during the first two cycles was conducted (Fig. 3a). During the charging, the 003 and 006 peaks shift towards lower angles resulting from the expansion of the layer distance between alternating (Cr, Ti)O_2 layers and the peaks return back to their original position on subsequent discharge, indicating highly reversible changes as electrode materials. Continuous changes in the peak positions, suggesting single phase reaction and solid solution formation, are found, except for the plateau region around 2.9 V, which is indicative of two-phase coexistence at the start of charge. Non-continuous change in the diffraction lines at the 2.9 V plateau region is clearly observed for the 006 diffraction line at 27.8 degrees. Simultaneously, the peak intensity of the 10l diffraction lines, especially for the 105 line at 42.3 degrees, is reduced on charge beyond this voltage plateau. Note that the peak intensity is recovered after the end of discharge. Because the prismatic sites are energetically stabilized by the presence of large K^+ ions, K^+ ion extraction induces phase transition and generally P3 to O3 phase transition is observed.[15] P3 to O3 phase transition is confirmed by the disappearance of the 105 peak for the P3 phase and the simultaneous appearance of the 104 peak corresponding to the O3 phase.[12] Unfortunately, the peak position of a Be window used for the *in situ* cell coincides with the position of the 104 peak at 41 degrees (Fig. S3, ESI†). Therefore, additional *ex situ* XRD data were collected during the charging process. Fig. S4 (ESI†) shows the simulated XRD

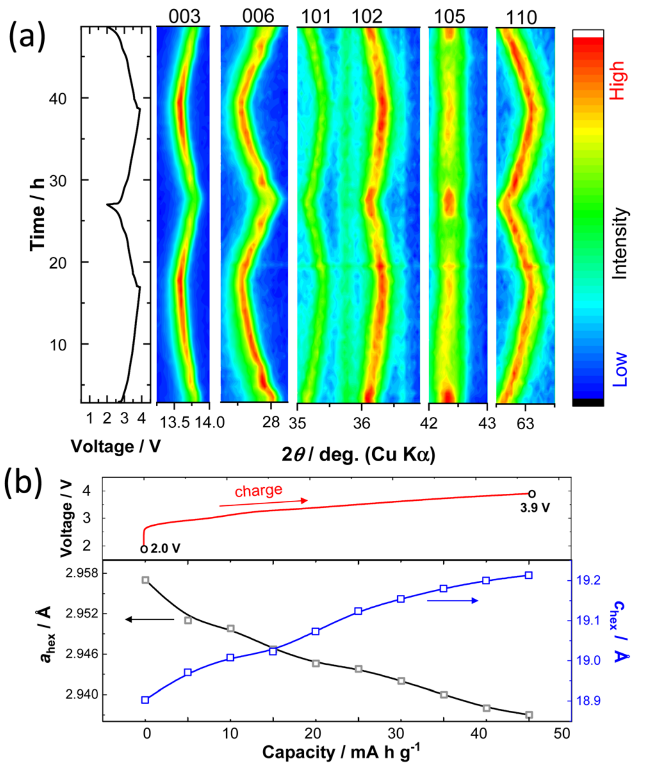

Fig. 3 Structural changes of $K_{0.6-y}Cr_{0.6}Ti_{0.4}O_2$ during charge/discharge; (a) the contour plots of *in situ* XRD data during the first two cycles in the voltage range of 2.0–3.9 V at a rate of 4 mA g^{-1}. The voltage change of the *in situ* cell is also shown. (b) Lattice parameter variations during the 2nd charge cycle.

patterns of $K_{0.6}Cr_{0.6}Ti_{0.4}O_2$ with P3- and O3-type structures and the presence of 104 or 105 peaks can differentiate between the two layered phases. The experimentally observed *ex situ* XRD patterns for the charged samples are also shown in Fig. S4 (ESI†). The 104 peak does not appear during charging to 3.9 V, suggesting that the P3 phase is retained on cycling and no phase transition to the O3 phase is evidenced. However, the broadening of the 105 peak suggests that stacking faults, probably associated with the partial formation of the O3 phase, are induced along the *c*-axis direction after K^+ ion extraction.[29] The lattice parameter changes upon charging during the 2nd cycle are also shown in Fig. 3b. The *c*-axis lattice parameter increases on charging because the K^+ ion extraction results in the increased electrostatic repulsion of the (Cr, Ti)O_2 layers and the expansion of the interlayer distance. From the *in situ* XRD patterns, although the co-existence of two distinct P3 phases with different interlayer distances is noted at the start of charge, averaged interlayer distances are plotted in Fig. 3b for simplicity. On the other hand, the *a*-axis lattice parameter decreases as the in-plane K^+–K^+ repulsive electrostatic interaction is reduced. The overall change in unit cell volume is relatively small, ∼0.27% in the voltage range of 2.0–3.9 V, leading to good capacity retention as an electrode material. The volume change during charge/discharge is one of the lowest among electrode materials for KIBs reported so far (Table S2, ESI†). The structural changes were further examined by an *in situ* XRD study with a higher voltage cutoff of 4.3 V (Fig. S5, ESI†). Upon charging, the intensity of the 006 peak is significantly decreased above 3.9 V. Moreover, the peak intensity of the 105 line is not recovered after discharge. Such irreversibility of structural evolution is indicative of structural deterioration on charging above 3.9 V, resulting in inferior reversibility as an electrode material.

To further assess the practical feasibility of P3 $K_{0.6}Cr_{0.6}Ti_{0.4}O_2$ for battery applications, the long-term cyclability was also tested and the sample was cycled for 500 cycles in the potential range of 2.0–3.9 V at a rate of 40 mA g^{-1} (Fig. 4a). A reversible capacity of 30 mA h g^{-1} is retained (*i.e.*, 98% of initial capacity) after 500 cycles along with 99.7% Coulombic efficiency for charge/discharge cycles. The selected charge/discharge curves (200th, 300th, 400th, and 500th cycles) provided in Fig. 4b show no significant change attesting to the remarkable structural stability of $K_{0.6}Cr_{0.6}Ti_{0.4}O_2$ against repeated K^+ ion insertion/deinsertion. The fast K^+ ion conduction due to low solvation energy associated with lower charge density for large K^+ ions is evidenced by the rate capability test (Fig. 4c). A discharge capacity of 30 mA h g^{-1} is achieved even at a rate of 640 mA g^{-1}. Although the reversible capacity of $K_{0.6}Cr_{0.6}Ti_{0.4}O_2$ (40 mA h g^{-1}) is smaller compared with that of $KCrO_2$ (80 mA h g^{-1}), the higher operating voltage ($E_{\text{ave.}}$ = 3.14 V for $K_{0.6}Cr_{0.6}Ti_{0.4}O_2$ *vs.* ∼2.5 V for $KCrO_2$[19]) coupled with superior durability is advantageous to design a full cell with graphite. The combination of average potential and reversibility makes $K_{0.6}Cr_{0.6}Ti_{0.4}O_2$ an attractive positive electrode in comparison to other positive electrodes for KIBs (Table S3, ESI†).

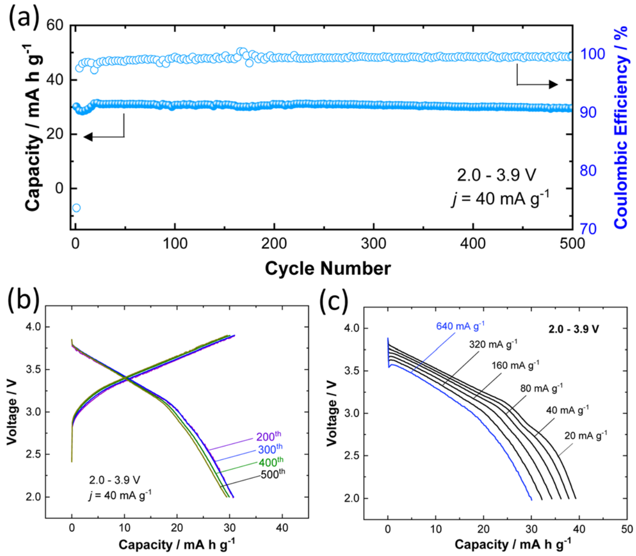

Fig. 4 Electrochemical properties of $K_{0.6}Cr_{0.6}Ti_{0.4}O_2$ as a potential positive electrode material for KIBs; (a) cycling stability for 500 cycles in the potential range of 2.0–3.9 V, (b) corresponding charge/discharge curves at the 200th, 300th, 400th, and 500th cycles, and (c) rate capability (active material mass loading: 2.16 mg cm^{-2}).

In summary, we have successfully synthesized phase pure P3-type $K_{0.6}Cr_{0.6}Ti_{0.4}O_2$ *via* a facile solid-state route. Without any optimization for particle size and morphology, it has delivered a reversible capacity of 43 and 30 mA h g^{-1} at a current rate of 5 and 640 mA g^{-1}, respectively, with excellent capacity retention. This compound with reversible Cr redox was found to show less pronounced phase transition on K^+ ion (de)insertion processes when compared with other layered oxides, which is beneficial for long life operation. Because Cr ions are not used as electrode materials for lithium battery applications, Cr-based layered oxides could be potentially used for potassium/sodium battery applications. This research progress will lead to the development of cost-effective and high-performance KIBs with moderate energy density in the future.

Conflicts of interest

There are no conflicts to declare.

Acknowledgements

This work has been partially supported by JSPS, Grant-in-Aid for Scientific Research (Grant Numbers 19H05816 and 21H04698), and JST, CREST Grant Number JPMJCR21O6, Japan. We thank Dr Yoshinobu Miyazaki and Dr Tomohiro Saito from Sumika Chemical Analysis Service, Ltd for the STEM observation. We thank Dr Debasmita Dwibedi for partial support of manuscript preparation.

References

1 L. Mauler, X. Lou, F. Duffner and J. Leker, *Energy Adv.*, 2022, **1**, 136–145.
2 B. D. L. Campéon and N. Yabuuchi, *Chem. Phys. Rev.*, 2021, **2**, 041306.

3 J. C. Pramudita, D. Sehrawat, D. Goonetilleke and N. Sharma, *Adv. Energy Mater.*, 2017, **7**, 1602911.

4 L. Fan, Y. Hu, A. M. Rao, J. Zhou, Z. Hou, C. Wang and B. Lu, *Small Methods*, 2021, **5**, 2101131.

5 Z. Jian, W. Luo and X. Ji, *J. Am. Chem. Soc.*, 2015, **137**, 11566–11569.

6 D. Igarashi, K. Kubota, T. Hosaka, R. Tatara, T. Inose, Y. Ito, H. Inoue, M. Takeuchi and S. Komaba, *Electrochemistry*, 2021, **89**, 433–438.

7 K. Kubota, *Electrochemistry*, 2020, **88**, 507–514.

8 W. Xu, H. Wang, Y. Gao, Y. Wei, H. Zhang, C. Gao, F. Kang and D. Zhai, *Energy Adv.*, 2022, **1**, 191–196.

9 T. Hosaka, K. Kubota, A. S. Hameed and S. Komaba, *Chem. Rev.*, 2020, **120**, 6358–6466.

10 H. Kim, J. C. Kim, M. Bianchini, D. H. Seo, J. Rodriguez-Garcia and G. Ceder, *Adv. Energy Mater.*, 2018, **8**, 1702384.

11 C. Vaalma, G. A. Giffin, D. Buchholz and S. Passerini, *J. Electrochem. Soc.*, 2016, **163**, A1295.

12 H. Kim, D. H. Seo, J. C. Kim, S. H. Bo, L. Liu, T. Shi and G. Ceder, *Adv. Mater.*, 2017, **29**, 1702480.

13 Y. Hironaka, K. Kubota and S. Komaba, *Chem. Commun.*, 2017, **53**, 3693–3696.

14 H. Kim, J. C. Kim, S. H. Bo, T. Shi, D. H. Kwon and G. Ceder, *Adv. Energy Mater.*, 2017, **7**, 1700098.

15 J.-Y. Hwang, J. Kim, T.-Y. Yu, S.-T. Myung and Y.-K. Sun, *Energy Environ. Sci.*, 2018, **11**, 2821–2827.

16 N. Naveen, S. C. Han, S. P. Singh, D. Ahn, K.-S. Sohn and M. Pyo, *J. Power Sources*, 2019, **430**, 137–144.

17 K. Sada and P. Barpanda, *Chem. Commun.*, 2020, **56**, 2272–2275.

18 X. Wang, X. Xu, C. Niu, J. Meng, M. Huang, X. Liu, Z. Liu and L. Mai, *Nano Lett.*, 2017, **17**, 544–550.

19 H. Kim, D.-H. Seo, A. Urban, J. Lee, D.-H. Kwon, S.-H. Bo, T. Shi, J. K. Papp, B. D. McCloskey and G. Ceder, *Chem. Mater.*, 2018, **30**, 6532–6539.

20 Z. Zhang, J. Sun, L. Duan, Y. Du, J. Li, J. Shen and X. Zhou, *J. Mater. Chem. A*, 2022, **10**, 554–560.

21 L. Duan, Y. Xu, Z. Zhang, J. Xu, J. Liao, J. Xu, Y. Sun, Y. He and X. Zhou, *J. Mater. Chem. A*, 2021, **9**, 22820–22826.

22 C. Delmas, C. Fouassier and P. Hagenmuller, *Physica B+C*, 1980, **99**, 81–85.

23 N. Ikeda, I. Konuma, H. B. Rajendra, T. Aida and N. Yabuuchi, *J. Mater. Chem. A*, 2021, **9**, 15963–15967.

24 F. Izumi and K. Momma, *Solid State Phenom.*, 2007, **130**, 15–20.

25 K. Momma and F. Izumi, *J. Appl. Crystallogr.*, 2011, **44**, 1272–1276.

26 T. Masese, Y. Miyazaki, G. Mbiti Kanyolo, T. Takahashi, M. Ito, H. Senoh and T. Saito, *ACS Appl. Nano Mater.*, 2021, **4**, 279–287.

27 Y. Tsuchiya, K. Takanashi, T. Nishinobo, A. Hokura, M. Yonemura, T. Matsukawa, T. Ishigaki, K. Yamanaka, T. Ohta and N. Yabuuchi, *Chem. Mater.*, 2016, **28**, 7006–7016.

28 R. Umezawa, Y. Tsuchiya, T. Ishigaki, H. B. Rajendra and N. Yabuuchi, *Chem. Commun.*, 2021, **57**, 2756–2759.

29 C. Delmas and C. Tessier, *J. Mater. Chem.*, 1997, **7**, 1439–1443.